CrossMark

J. Fluid Mech. (2019), *vol.* 873, *pp.* 508–530. © Cambridge University Press 2019
doi:10.1017/jfm.2019.424

Observation of surface wave patterns modified by sub-surface shear currents

Benjamin K. Smeltzer[1], **Eirik Æsøy**[1] **and Simen Å. Ellingsen**[1,†]

[1]Department of Energy and Process Engineering, Norwegian University of Science and Technology, N-7491 Trondheim, Norway

(Received 8 November 2018; revised 22 May 2019; accepted 22 May 2019; first published online 25 June 2019)

We report experimental observations of two canonical surface wave patterns – ship waves and ring waves – skewed by sub-surface shear, thus confirming effects predicted by recent theory. Observed ring waves on a still surface with sub-surface shear current are strikingly asymmetric, an effect of strongly anisotropic wave dispersion. Ship waves for motion across a sub-surface current on a still surface exhibit striking asymmetry about the ship's line of motion, and large differences in transverse wavelength for upstream versus downstream motion are demonstrated, all of which is in good agreement with theoretical predictions. Neither of these phenomena can occur on a depth-uniform current. A quantitative comparison of measured versus predicted average phase shift for a ring wave is grossly mispredicted by no-shear theory, but in good agreement with predictions for the measured shear current. A clear difference in wave frequency within the ring wave packet is observed in the upstream versus downstream direction for all shear flows, while wave dispersive behaviour is identical to that for quiescent water for propagation normal to the shear current, as expected. Peak values of the measured two-dimensional Fourier spectrum for ship waves are shown to agree well with the predicted criterion of stationary ship waves, with the exception of some cases where results are imperfect due to the limited wavenumber resolution, transient effects and/or experimental noise. Experiments were performed on controlled shear currents created in two different ways, with a curved mesh and beneath a blocked stagnant-surface flow. Velocity profiles were measured with particle image velocimetry, and surface waves with a synthetic schlieren method. Our observations lend strong empirical support to recent predictions that wave forces on vessels and structures can be greatly affected by shear in estuarine and tidal waters.

Key words: coastal engineering, shear waves, surface gravity waves

1. Introduction

Ship waves and ring waves have been admired since the dawn of time, and studied scientifically for two centuries (Wehausen & Laitone 1960), pioneered by Poisson (1816), Cauchy (1827) and Kelvin (Thomson 1887). Observations of their modification by sub-surface shear flows, however, have not been reported, despite the abundance of

† Email address for correspondence: simen.a.ellingsen@ntnu.no

https://doi.org/10.1017/jfm.2019.424 Published online by Cambridge University Press

flows with strong vertical shear in nature, for instance beneath the windswept ocean surface and in coastal and riverine waters. In these waters understanding the physics of surface waves can be crucial to a wide range of problems, including wave loads on vessels and installations, transportation of nutrients and pollutants and thermal mixing, a key factor in climate modelling (Belcher *et al.* 2012). It has long been recognized that surface waves are profoundly affected by sub-surface shear (Peregrine 1976), yet only recently has sub-surface shear been implemented in widely used ocean models (Kumar, Voulgaris & Warner 2011; Elias, Gelfenbaum & van der Westhuysen 2012), and remote sensing of near-surface shear currents has been a point of attention in the last few years (Lund *et al.* 2015; Campana *et al.* 2016).

Recent theory has predicted that ship and ring waves are affected in striking ways by sub-surface shear; for instance, ring waves, such as from a pebble thrown into the water, no longer form concentric rings (Johnson 1990; Ellingsen 2014*b*; Khusnutdinova & Zhang 2016), and Kelvin's famous result that ship waves in deep water always form an angle of approximately 39° no longer holds (Ellingsen 2014*a*; Li & Ellingsen 2016). The physical understanding of ship waves more generally has been the focus of much recent attention (Rabaud & Moisy 2013; Darmon, Benzaquen & Raphaël 2014; Noblesse *et al.* 2014; Pethiagoda, McCue & Moroney 2014; Caplier *et al.* 2015).

In the strongly sheared waters of the Columbia River delta – often called 'the Graveyard of the Pacific' for its dangerous sailing conditions and many shipwrecks – the steepness of breaking waves was recently found by Zippel & Thomson (2017) to be mispredicted by up to 20 % unless shear was accounted for. In the same waters the wave-making resistance on smaller ships, typically accounting for more then 30 % of fuel consumption (Faltinsen 2005), was found to differ by a factor 3 or more between upstream and downstream motion at the same typical operational velocity relative to the water surface (Li, Smeltzer & Ellingsen 2019). Studying wave forces during hurricanes theoretically 45 years ago, Dalrymple (1973) found large shear effects and concluded that 'It is obvious ... that rational offshore design must include the effect of [shear] currents'. This, however, is still not the practice today.

In this article we report observations of ring waves and ship waves skewed by shear – the first to our knowledge – and show that these are well described by recently developed theory. In the following we briefly review the theory for calculating linear wave patterns on shear currents of arbitrary profiles, for comparison with our measurements. We next describe the experimental set-up, whereupon observations of ring waves and ship waves are presented and discussed, in that order. We conclude with a discussion of implications of the results in a wider context. Supplementary movie 1, available at https://doi.org/10.1017/jfm.2019.424, further visualises the striking effect of shear observed for both types of wave patterns.

2. Theoretical prediction of wave patterns

We will briefly review the theoretical framework for the calculation of transient, general linear wave patterns propagating upon a horizontal shear current of arbitrary velocity profile, formulated in a manner suited for the present purposes. The theory, suitable for ship waves in particular, was first developed for stationary ship waves by Smeltzer & Ellingsen (2017) and further generalized by Li *et al.* (2019). It assumes the source of the waves – in our case ship waves and ring waves – is a patch of pressure, $\hat{p}_{ext}(\boldsymbol{r}, t)$, of arbitrary shape in the horizontal plane $\boldsymbol{r} = (x, y)$, and arbitrary dependence on time t. The pressure is $P(\boldsymbol{r}, z, t) = -\rho g z + \hat{p}(\boldsymbol{r}, z, t)$, the vertical

https://doi.org/10.1017/jfm.2019.424 Published online by Cambridge University Press

displacement of the free surface is $\hat{\zeta}(\boldsymbol{r}, t)$ and the vertical velocity is $\hat{w}(\boldsymbol{r}, z, t)$; z is the vertical axis, g the gravitational acceleration and ρ the water density, assumed constant. We let the bottom be at $z = -h$, and the undisturbed surface be $z = 0$. Hatted quantities are presumed small, and governing equations and boundary conditions are linearized with respect to these; their corresponding quantities in the Fourier $\boldsymbol{k}$-plane are

$$[\hat{\zeta}, \hat{w}, \hat{p}](\boldsymbol{r}, z, t) = \int \frac{\mathrm{d}^2 k}{(2\pi)^2} [\zeta, w, p](z, t; \boldsymbol{k}) \mathrm{e}^{\mathrm{i}\boldsymbol{k}\cdot\boldsymbol{r}}, \tag{2.1}$$

(it is understood that $\hat{\zeta}$ and ζ are not functions of z). We denote the wave vector $\boldsymbol{k} = (k_x, k_y)$ so that $k = |\boldsymbol{k}|$. We assume unidirectional ambient current $\boldsymbol{U}(z) = U(z)\boldsymbol{e}_x$ along the x-axis. Numerically, inverse Fourier transforms are calculated with the inverse fast Fourier transform method (iFFT). In the following the dependence on $\boldsymbol{k}$ of quantities in phase space is implied.

Eliminating horizontal velocity components from the linearized Euler equation according to the standard procedure (cf. e.g. Shrira 1993) yields the boundary value problem

$$(\boldsymbol{k}\cdot\boldsymbol{U} - kc)(w'' - k^2 w) = \boldsymbol{k}\cdot\boldsymbol{U}'' w; \quad -h < z < 0, \tag{2.2a}$$

$$(\boldsymbol{k}\cdot\boldsymbol{U} - kc)^2 w' - \left(gk^2 + \frac{\sigma k^4}{\rho}\right) w - \boldsymbol{k}\cdot\boldsymbol{U}'(\boldsymbol{k}\cdot\boldsymbol{U} - kc) w = 0; \quad z = 0, \tag{2.2b}$$

$$w = 0; \quad z = -h, \tag{2.2c}$$

where it is understood that the perturbation quantities have time dependence $\exp[-\mathrm{i}\omega(\boldsymbol{k})t]$, $c = \omega/k$ is the phase velocity and σ the surface tension coefficient. The prime superscripts indicate a differentiation with respect to z. Using (2.2*a*) the boundary condition (2.2*b*) can be combined into the implicit form of the dispersion relation (Ellingsen & Li 2017)

$$(1 + I)(kc - \boldsymbol{k}\cdot\boldsymbol{U}_0)^2 + (kc - \boldsymbol{k}\cdot\boldsymbol{U}_0)\boldsymbol{k}\cdot\boldsymbol{U}_0' \tanh kh/k - k^2 c_0(k)^2 = 0, \tag{2.3}$$

where

$$I = \int_{-h}^{0} \mathrm{d}z \frac{\boldsymbol{k}\cdot\boldsymbol{U}''(z) w(z, 0) \sinh k(z + h)}{k(\boldsymbol{k}\cdot\boldsymbol{U} - kc) w(0, 0) \cosh kh}. \tag{2.4}$$

Here $c_0(k) = \sqrt{(g/k + \sigma k/\rho)\tanh kh}$, $\boldsymbol{U}_0 = \boldsymbol{U}(0)$ and $\boldsymbol{U}_0' = \boldsymbol{U}'(0)$.

The resulting eigenvalues of c are $c_\pm(\boldsymbol{k})$ and due to the relation $c_-(\boldsymbol{k}) = -c_+(-\boldsymbol{k})$, only the positive value $c_+(\boldsymbol{k})$ is needed. For a general arbitrary profile $U(z)$, an explicit form of the dispersion relation cannot be expressed since both c and $w(z, t)$ are unknown and (2.3) and (2.4) are not closed. There exists a number of different ways to approximate $c_+(\boldsymbol{k})$ from an arbitrary $U(z)$, either numerically or using approximate analytical expressions – for a review, see Li & Ellingsen (2019) – and how one chooses to calculate $c_+(\boldsymbol{k})$ is of no significance other than numerical cost and accuracy requirements. At the level of accuracy required for our present purposes an analytical approximation such as that of Stewart & Joy (1974) for deep water would likely be adequate, yet introducing this additional source of error is unnecessary since we might instead employ, with little additional cost or complexity,

https://doi.org/10.1017/jfm.2019.424 Published online by Cambridge University Press

the arbitrary-accuracy direct-integration method (DIM) of Li & Ellingsen (2019). We hence assume $c_\pm(\boldsymbol{k})$ to be known functions henceforth.

The surface elevation has contributions from waves created at all previous times via a propagator function (Green function) H_ζ,

$$\zeta(\boldsymbol{k}, t) = \int_{-\infty}^{t} \mathrm{d}\tau p_{ext}(\boldsymbol{k}, \tau) H_\zeta(\boldsymbol{k}, t-\tau), \tag{2.5}$$

hence all that is required is finding H_ζ. It is shown by Li *et al.* (2019) that the solution may be written

$$H_\zeta(\boldsymbol{k}, t) = \frac{\tanh kh}{\mathrm{i}\rho(c_+ - c_-)(1+I)}(\mathrm{e}^{-\mathrm{i}kc_+ t} - \mathrm{e}^{-\mathrm{i}kc_- t}), \tag{2.6}$$

where $c_\pm$ are functions of $\boldsymbol{k}$. Once $c_+(\boldsymbol{k})$ is known, $w(z)$ is found from (2.2*a*) and I is calculated. (An advantage of using the DIM method of Li & Ellingsen (2019) is that it builds on the same relations and yields I together with c_+ automatically.)

If one assumes a stationary ship wave pattern, equation (2.5) can be simplified to

$$\zeta(\boldsymbol{r}) = \frac{1}{\rho}\lim_{\epsilon\to+0}\int \frac{\mathrm{d}^2k}{(2\pi)^2}\frac{p_{ext}(\boldsymbol{k})\tanh kh}{k(1+I)(c_+ - \mathrm{i}\epsilon)(c_- - \mathrm{i}\epsilon)}\exp(\mathrm{i}\boldsymbol{k}\cdot\boldsymbol{r}), \tag{2.7}$$

where a radiation condition has been applied. We use the fully transient expression however, to account for the linear acceleration phase of our model ship, since the transient wave pattern from this phase is visible in our experimental results for the two lowest Froude numbers we consider.

Our ship wave predictions use a hyper-Gaussian shape for the ship,

$$\hat{p}_{ext}(\boldsymbol{r}) = p_0 \exp\{-\pi^2[(2x_\beta/L)^2 + (2y_\beta/b)^2]^3\}, \tag{2.8}$$

where the length and beam of the model ship are, respectively, $L = 110$ mm and $b = 16$ mm, and x_β, y_β are coordinates relative to the ship with x_β as the forward direction.

For the initial value (ring wave) problem, a simpler form is more suitable. In fact, defining initial conditions for waves on shear currents in a fully consistent manner is a subtle affair, as discussed by Akselsen & Ellingsen (2019), since some assumption must be made about the initial perturbation to the sub-surface vorticity field. However, we use the simplest choice, as used by Ellingsen (2014*b*) (Ellingsen (2014*b*) erroneously argued that this choice is necessary; see Akselsen & Ellingsen (2019)) which makes for the following simple argument. We note that if $\hat{p}_{ext}(\boldsymbol{r}, t)$ is supposed to be a short impulse at $t = t_0$, $\hat{p} \propto \delta(t - t_0)$, the surface elevation (2.5) obtains the form (see Li *et al.* (2019))

$$\zeta(\boldsymbol{k}, t) = Z_+(\boldsymbol{k})\mathrm{e}^{-\mathrm{i}kc_+(\boldsymbol{k})(t-t_0)} + Z_-(\boldsymbol{k})\mathrm{e}^{-\mathrm{i}kc_-(\boldsymbol{k})(t-t_0)} \tag{2.9}$$

for $t > t_0$, with $Z_\pm$ as undetermined coefficients. It follows that any freely propagating wave pattern will be of this form once the source is 'switched off'. Assuming the surface elevation is known at $t = t_0$ to be $\hat{\zeta}(\boldsymbol{r}, 0) = \zeta_0(\boldsymbol{r})$ and $\partial\hat{\zeta}(\boldsymbol{r}, 0)/\partial t = \dot{\zeta}_0$, equation (2.1) yields

$$Z_\pm(\boldsymbol{k}) = \mp\frac{kc_\mp\zeta_0(\boldsymbol{k}) - \mathrm{i}\dot{\zeta}_0(\boldsymbol{k})}{k[c_+(\boldsymbol{k}) - c_-(\boldsymbol{k})]}. \tag{2.10}$$

https://doi.org/10.1017/jfm.2019.424 Published online by Cambridge University Press

2.1. *Initial conditions for the prediction of ring waves*

The initial conditions used for comparison with experiment are the values of ζ_0 and $\dot{\zeta}_0$ at the earliest time where measurements are available. The surface elevation is found from the measured surface gradient field, sampled at discrete points in time (detail provided in § 3), and $\dot{\zeta}_0$ may be approximated using a central difference scheme from the values of ζ at adjacent sampled points in time, accurate to second order in the small parameter $f_s T$, where f_s is the camera sample rate and T a characteristic time scale for the ring wave development. The approximation of $\dot{\zeta}_0$ is further improved using an algorithm similar to Gerchberg–Saxton (GS) (cf., e.g. Fienup 1982). The central difference approximation to $\dot{\zeta}_0$ is taken as an initial guess, and used with ζ_0 in (2.9) to propagate forward a value $t_s = f_s^{-1}$ in time to the next sampled surface elevation. The resulting calculated surface elevation is replaced by the measured values in (2.10), whereby (2.9) is used to propagate backwards a time t_s. The measured surface elevation is again substituted into (2.10), and the entire process repeated multiple times. Since the surface elevation at subsequent times is determined by ζ_0 and $\dot{\zeta}_0$, the method effectively finds the unknown $\dot{\zeta}_0$ from measurements of the surface elevation at two points in time.

3. Laboratory set-up

The laboratory set-up is shown schematically in figure 1. Shear currents were generated in a laboratory wave tank using a pump system to induce flow over a transparent plate of dimension 2 m $\times$ 2 m. The vertical profile of the streamwise current was measured using a particle image velocimetry (PIV) system similar to that described in Willert *et al.* (2010), consisting of a high power LED light source (Luminus PT-120-TE), fibre array and collimation lens to produce a pulsed light sheet. This PIV system was able to measure the velocity profile at any location in a measurement area of approximately 50 cm $\times$ 50 cm. The water was seeded with 40 μm polystyrene spheres (Microbeads AS) and the streamwise fluid velocity component was obtained by processing images from a camera (Imperx Bobcat 1610) mounted out of the plane as shown in figure 1. The position of the light sheet can be moved to any location in the measurement area. The free-surface elevation was measured using a synthetic schlieren (SS) method similar to that of Moisy, Rabaud & Salsac (2009), imaging a random dot pattern mounted below the transparent plate (optical path length $\approx$2 m) at a frame rate of 35 Hz. Images were processed using a windowed digital image correlation technique, where the displacement of the dots relative to a still-water reference determines the local free-surface gradient, with horizontal spatial resolution of 5.7 mm. The free-surface elevation was found as the solution to an overdetermined linear system formed by expressing the gradients at each measurement point as second-order central differences in terms of the unknown surface elevation values (Moisy *et al.* 2009). The value of the surface elevation at a corner of the spatial domain was set to zero (effectively a necessary integration constant). As a result, there is a time-dependent offset in the mean surface elevation when waves pass over the corner point. The time-dependent offset is later removed by filtering, as described below.

The uncertainty in the measured gradients was estimated to be 0.001 or less in magnitude, based on analysis of a sequence of images taken with a still-water surface. To estimate the corresponding error in the reconstructed surface elevation, an empirical law proposed by Moisy *et al.* (2009) was used. Assuming a root-mean-square (r.m.s.) wave slope of 0.02 (a typical value, see e.g. figure 6*a–d*) and thus a relative

https://doi.org/10.1017/jfm.2019.424 Published online by Cambridge University Press

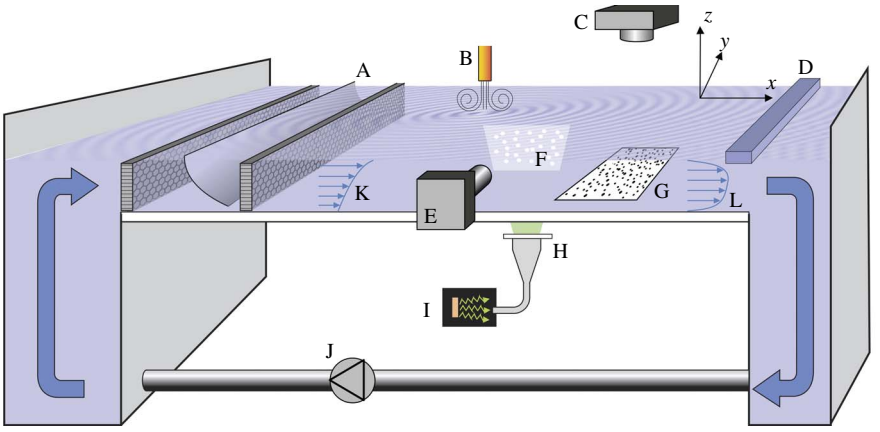


FIGURE 1. (Colour online) Laboratory set-up. A: curved mesh and honeycomb flow straighteners; B: pneumatic wave maker; C: schlieren camera; D: stagnation bar; E: PIV camera; F: PIV light sheet; G: random dot pattern; H: collimation lens; I: LED light source; J: pump; K: shear profile due to curved mesh; L: stagnation shear profile.

uncertainty of 5 % in the measured gradients, the fractional error in the surface elevation was estimated to be 5 % for a 2.5 cm wavelength, and 1 % for a 10 cm wavelength. It is noted than in isolated regions of the measurement area containing waves with high curvature (particularly short wavelengths), larger errors may result due to lens effects of the dot pattern (Moisy *et al.* 2009).

To remove the offset in mean surface elevation as well as other noise, the data were filtered to remove periodic components that do not approximately satisfy the linear dispersion relation $\omega_0(\boldsymbol{k})$ in quiescent waters, allowing for deviations as expected due to the shear currents. The filter F was defined in wave vector–frequency Fourier space of the surface elevation as

$$F(\boldsymbol{k}, \omega) = \exp\left[-\left(\frac{\omega - \omega_0(\boldsymbol{k})}{U_{max}k}\right)^4\right], \tag{3.1}$$

where ω is the frequency, $k = |\boldsymbol{k}|$ and U_{max} is a maximum expected current. The surface elevation and gradient fields were filtered by taking the Fourier transform in spatial dimensions and time, multiplying the result by (3.1), and performing an inverse Fourier transform of the product back to the spatial–temporal domain. The filter removes periodic components that lie outside a frequency range $U_{max}k$ from the quiescent-water dispersion relation. The value of U_{max} was chosen in practice to be ≈ 0.05 ms^{-1} larger than the maximum current measured by PIV.

Shear current profiles were created in two ways, each producing conditions with good streamwise and spanwise homogeneity within the measurement area. Firstly, similar to the method of e.g. Dunn & Tavoularis (2007), a curved mesh at the inlet was used to create a moderately sheared current of approximately linear profile with vorticity vector along the positive y-axis, as shown in figure 1(*b*). Secondly, an area exists covering roughly the downstream half of the tank, where the surface is stagnant in the laboratory frame of reference, with the flow dipping suddenly beneath it, developing a surface boundary layer. This 'stagnation region' stretches across the spanwise range and reaches up to a sharp spanwise separation line – a Reynolds

https://doi.org/10.1017/jfm.2019.424 Published online by Cambridge University Press

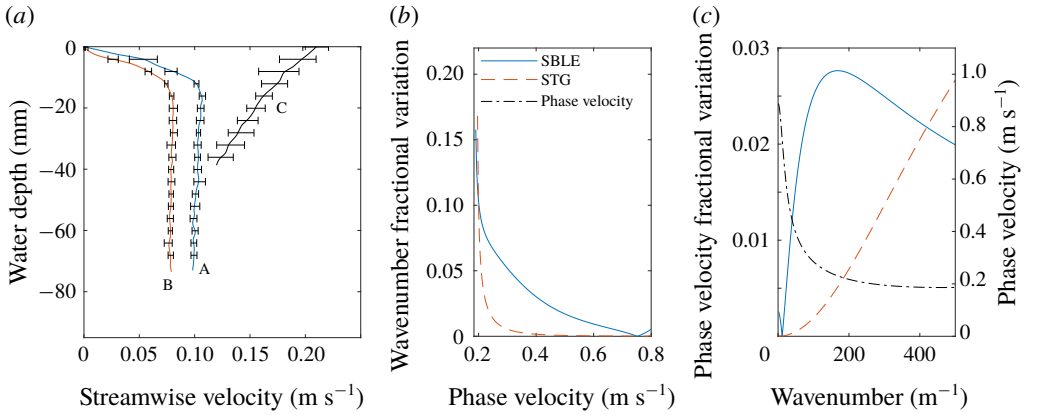


FIGURE 2. (Colour online) (*a*) Measured velocity field in stagnation region (profiles A and B) and downstream of curved mesh (profile C). (*b*) Fractional variation of the wavenumber as a function of phase velocity across the measurement region due to inhomogeneity in the dispersion relation caused by the surface boundary layer evolution (SBLE) and surface tension gradients (STG). (*c*) Fractional variation in the phase velocity as a function wavenumber for the same cases as (*b*). Also shown in (*c*) is the phase velocity for which the rightmost vertical axis applies. Downstream (shear-assisted) propagating waves are considered. The legend in (*b*) applies to (*b*,*c*).

ridge (Scott 1982) – some 80 to 200 cm upstream, depending on flow rate and the concentration of surface contaminants. The area can be moved further upstream with the simple placement of a horizontal spanwise bar dipping slightly beneath the surface.

The velocity profiles used herein, measured with PIV, are shown in figure 2(*a*) for stagnation region profiles (A and B) and the flow due to the curved mesh (profile C). Error bars show maximum and minimum values within the measurement area measured at four points, one in each quadrant, with the graph showing the average. The streamwise variation of the shear profiles A and B is in rough agreement with the expected boundary layer thickness as a function of distance downstream from the Reynolds ridge. The water depth was 95 mm for stagnation region flow, and 50 mm for curved mesh flow; velocity profiles were not measured for the bottom 15 mm or so, yet the relevant wave spectra have hardly any contribution from waves long enough to be influenced by the bottom boundary layer.

Ring waves were produced using a pneumatic wave maker discharging bursts of air onto the surface, causing negligible disruption of the ambient current. The air flow nozzle has diameter 1.0 mm and was positioned 50–100 mm above the water surface, and the air flow was controlled by a solenoidal valve in 50 ms pulses. For the curved mesh flow, profile C of figure 2(*a*), the nozzle was moved along with the flow at the surface velocity using a linear stage. Ship waves were generated by mounting a miniature hull (Series 60) on a linear stage to move the ship at constant speed at different angles to the shear current. After initial acceleration of 1 ms^{-2}, velocity variations were found to be less than 1 % of the design speed.

The surface tension coefficient was determined by measuring waves produced by pulsing the pneumatic wave maker at frequencies in the range 5–10 Hz in otherwise quiescent water, and analysing the wavenumber–frequency spectrum obtained by performing a discrete fast Fourier transform in space and time, where peaks in the

https://doi.org/10.1017/jfm.2019.424 Published online by Cambridge University Press

spectrum are expected to lie on the linear dispersion surface. A set of points $\{\omega_i, k_i\}$ were extracted from the data at wave frequencies ω_i by fitting a Gaussian function along various directions in k_x–k_y space to find the peak k_i of the spectral signal. The set of points was then fitted to the function $\omega(k) = \sqrt{(gk + \Gamma k^3)\tanh kh}$, with Γ the free parameter representing the ratio of surface tension to fluid density.

In the stagnation region results, the concentration of surface contaminants is higher than in regions where the surface is moving as well as in quiescent water when the pump is turned off, and consequently the surface tension may be notably affected. To obtain representative values of the surface tension with the pump turned on, horizontal bars spanning the width of the tank and dipping beneath the surface were placed at the upstream and downstream boundaries of the wave measurement region prior to turning off the pump. Thus the contaminants were effectively prevented from spreading over the entire channel region and a representative measurement of surface tension could be made on the now quiescent water in the same way as described in the previous paragraph. Measurements were performed promptly after the pump was turned off such that any desorption of surfactants from the surface layer to the bulk water was minimized. It is noted that within the surface stagnation region there is in fact a surface tension gradient in the streamwise direction, which arises to balance the surface shear stress from the shear current (Harper & Dixon 1974). Using a value of the viscosity in clean water and typical measured values of the surface shear, the surface tension coefficient was estimated to vary by approximately 0.003 Nm^{-1} across the wave measurement region, or 3×10^{-6} $\mathrm{m}^3\ \mathrm{s}^{-2}$ in the value of Γ amounting to a relative variation of $\sim$10 % over the measurement area.

Both the variation of the surface tension as well as the shear flow within the measurement area contribute to an inhomogeneous wave dispersion relation with a slight x-dependence. It is noted that the dispersion relation is in addition anisotropic due to the shear flow. The theoretical predictions used herein assume a dispersion relation that is homogeneous in space. Measures of the variation in the dispersion relation at the upstream and downstream boundaries of the wave measurement area based on the measured variations in shear profile B representative of the surface boundary layer evolution (SBLE) as well as the estimated variation in surface tension due to the streamwise gradient (STG) are shown in figure 2(*b*,*c*). The fractional variation in wavenumber for a given phase velocity is shown in figure 2(*b*), while the variation in phase velocity as a function of wavenumber is shown in figure 2(*c*), where the leftmost vertical axis applies. Also shown in figure 2(*c*) is the phase velocity as a function of wavenumber (where the rightmost vertical axis applies) for reference, calculated assuming the average shear profile and surface tension coefficient over the measurement area. Downstream propagating waves are considered, although the trends are similar for upstream waves. For all but the shortest measured wavelengths, the surface boundary layer development has a greater effect on wave dispersion variation across the measurement domain. Given a minimum phase velocity of $\approx$0.19 ms^{-1}, the fractional error in wavenumber increases dramatically for phase velocities approaching the minimum value, where the phase velocity derivative with respect to wavenumber goes to zero. For measured ring waves, the surface boundary layer results in a $\leqslant$2.5 % variation in the phase evolution of a wave, resulting in wave components drifting slightly out of phase compared to theoretical predictions. In the context of ship waves measurements for relevant velocities of 0.3–0.6 ms^{-1}, there is a $\leqslant$5 % variation in the wavelength of the wave directly following ship. The variation in wave dispersion is expected to be one of the main causes of disagreement between experiment measurements and theoretical predictions shown in the following sections,

https://doi.org/10.1017/jfm.2019.424 Published online by Cambridge University Press

and is discussed further in the context of the quantitative results shown in §§ 5 and 6. The assumption of a homogeneous dispersion relation in the theory is deemed satisfactory for the level of accuracy of the present study, especially considering that disagreements caused by the variations shown in figure 2(*b*,*c*) are partially averaged out in quantitative metrics that analyse the waves over the entire measurement region.

The presence of increased surface contaminants in the stagnation region results in a thin viscoelastic surface film, which may notably increase the viscous damping of surface waves compared to water with a clean surface (Alpers & Hühnerfuss 1989). However, estimates of the damping from analysis of the wave measurements used in determining Γ showed no clear trends of increased damping rates relative to theoretical predictions based on the Stokes equation (Alpers & Hühnerfuss 1989) within the level of accuracy of the analysis. The inviscid theory presented in § 2 does not include damping effects (the phase velocities and wave vectors are assumed real quantities), which may contribute to a slight disagreement between experiments and theoretical predictions for the smallest wavelengths (a damping rate of $\sim 1\ \mathrm{m}^{-1}$ was estimated for a 2 cm wavelength, and $\sim 0.2\ \mathrm{m}^{-1}$ for a 4.5 cm wavelength using the lowest measured surface tension value). It is noted that measured damping rates could be included in the theory in § 2 as an imaginary component to $c_{\pm}(\boldsymbol{k})$ for use in potential future studies.

To avoid ambiguity we will use the convention of Li *et al.* (2019) and refer to shear-assisted (shear-inhibited) directions of motion, pointing along (against) the current direction in a reference system where the surface is at rest. In particular, the 'downstream' direction is shear assisted in the stagnation flow region (profiles A and B in figure 2*a*), but shear inhibited in the region behind the curved mesh (profile C in figure 2*a*) as the current velocity decreases with depth relative to the value at the surface for profile C.

4. Linear dispersion relation

We measured the dispersion relation for waves atop shear current profile A by driving omnidirectional waves approximately monochromatically over a range of frequencies, then Fourier transforming the surface gradients in time and space to obtain spectra $P_x(\boldsymbol{k}, \omega)$ and $P_y(\boldsymbol{k}, \omega)$ for the gradient components along the x and y-directions respectively, where ω is the frequency. The magnitudes squared of the spectra for each component are added together to produce a single spectrum shown in figure 3(*a*). The surface tension coefficient parameter was measured to be $\Gamma = 2.8 \pm 0.1 \times 10^{-5}\ \mathrm{m}^3\ \mathrm{s}^{-2}$. A clear maximum of the power spectrum is seen along the dispersion curve which is consistent with the dispersion relation $\omega(\boldsymbol{k})$ calculated numerically for the measured dispersion profile (solid line), but inconsistent with the quiescent-water prediction (dashed line). Theoretical predictions of the phase and group velocities in the shear-assisted and shear-inhibited directions are shown in figure 3(*b*) as a function of wavenumber. Due to the background shear current, there are distinct differences in the velocities depending on direction of wave propagation, indicating that wave patterns such as ring waves and ship waves explored in the following sections will be significantly modified.

5. Ring wave observations

Ring wave measurements atop the stagnation region flow profile A in figure 2(*a*) and corresponding theoretical predictions using (2.9) and (2.10) are shown in figure 4. We compare measurements in quiescent water (figure 4*i*–*l*) with those

https://doi.org/10.1017/jfm.2019.424 Published online by Cambridge University Press

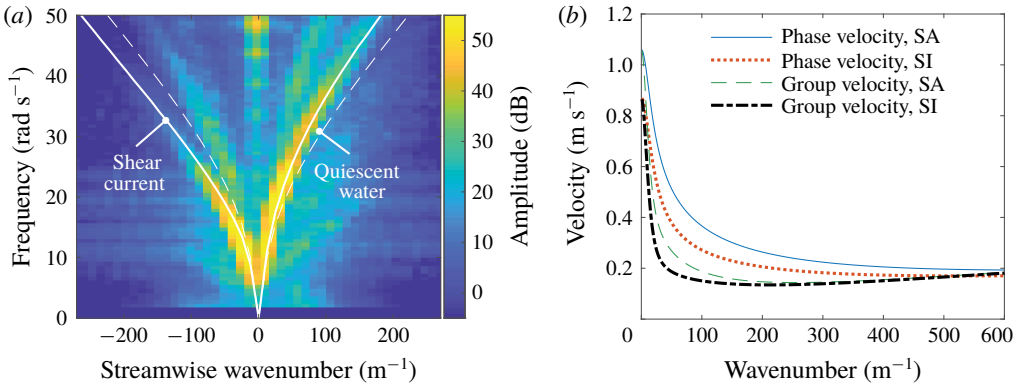


FIGURE 3. (Colour online) (*a*) Measured dispersion relation for the shear current in the stagnation region, profile A in figure 2(*a*), and theoretical predictions for quiescent water and shear current, respectively. (*b*) Calculated phase and group velocities for wave propagation in the shear-assisted (SA) and shear-inhibited (SI) directions atop the same shear profile.

made with the same initial pulse atop stagnation region shear profile A in figure 2(*a*) (figure 4*a–d*). Each column shows a particular time after the initial pulse, as indicated. The asymmetry compared to quiescent water is striking. Images of a ring wave propagating on the approximately linear shear current, profile C of figure 2(*a*), are shown in figure 5. The height of the pneumatic pressure pulse above the water surface is larger than for the stagnation region case, resulting in slightly longer wavelength components. Due to the weaker shear the asymmetry is less conspicuous, yet differences between streamwise and spanwise propagation are still apparent. Left and right in the image appear to be reversed compared to the stagnation flow case since vorticity now has the opposite sign. The surface velocity is non-zero for the mesh flow, so the whole pattern is convected downstream (towards the right); this amounts to a change of reference system and can cause no asymmetry of the pattern itself. Further quantitative analysis presented below confirms the observable effects of the subsurface shear current. To ensure no asymmetry could arise due to relative motion of the surface and wave maker, the pneumatic nozzle was moved along with the flow so as to follow the surface, using a linear stage.

As initial condition for the theoretical predictions, we use the measured surface elevation and velocity at the earliest available time, $t = 0.54$ s for stagnation region flow, and $t = 0.77$ s for the curved mesh profile. Before these times images are partly obscured by the pneumatic wave maker being within the field of vision. The coefficient representing the ratio of the surface tension coefficient to fluid density was found to be $\Gamma = 2.8 \pm 0.1 \times 10^{-5}$ m^3 s^{-2} for both the stagnation region and quiescent waters in figure 4, reported to two significant figures. This corresponds to a surface tension coefficient of 0.028 ± 0.001 Nm^{-1} for a density of 997 kg m^{-3}. The bounds indicate the 95 % confidence intervals of the fits. The stagnation region covered much of the length of the channel during the experiments, which is likely the reason the surface tension value is approximately unchanged when the pump was turned off. The parameter Γ was not measured for the case of the curved mesh profile, and a value of 7×10^{-5} m^3 s^{-2} was used in the theoretical predictions, estimated based on other measurements of Γ during the time period where the experiments were conducted.

https://doi.org/10.1017/jfm.2019.424 Published online by Cambridge University Press

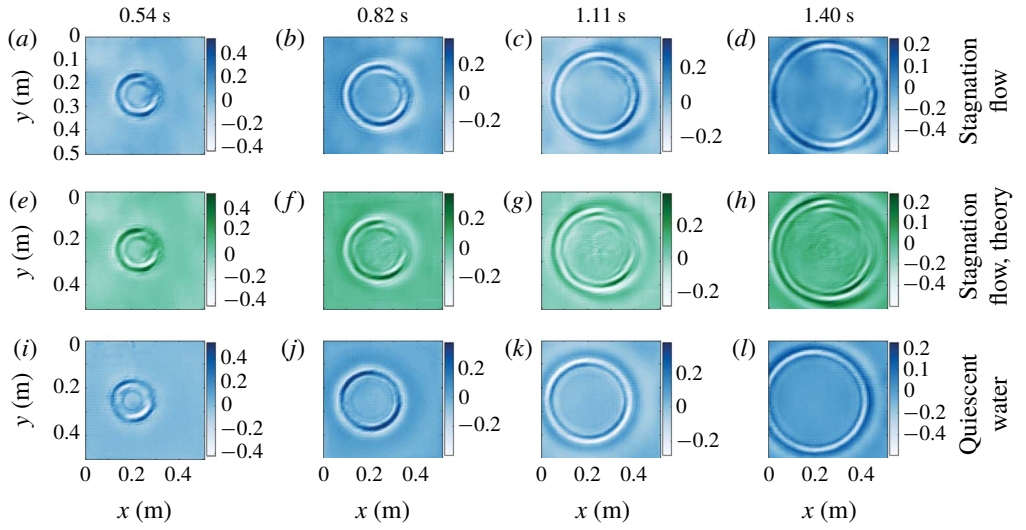


FIGURE 4. (Colour online) Ring waves, measured and predicted. Rows and columns respectively represent different cases and times after the initial pulse, as indicated. Blue-tinted panels (top and bottom rows) are measured, green tinted (middle row) are theoretical predictions. The current is from left to right in the laboratory frame of reference. The colour bars show the surface elevation in millimetres.

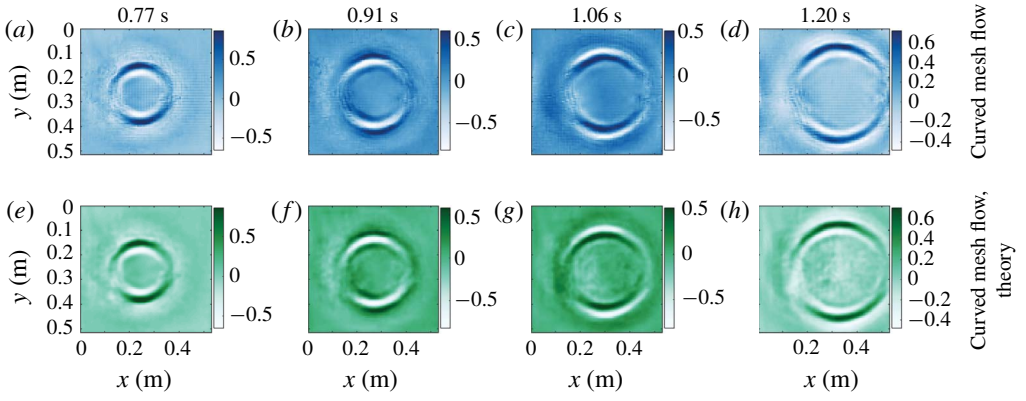


FIGURE 5. (Colour online) Ring waves, measured and predicted. Rows and columns respectively represent different cases and times after the initial pulse, as indicated. Blue-tinted panels (top row) are measured, green tinted (bottom row) are theoretical predictions. The current is from left to right in the laboratory frame of reference. The colour bars show the surface elevation in millimetres.

The theoretically predicted surface amplitude at each respective time is shown in figure 4(*e–h*) and 5(*e–h*) (green-tinted). Agreement with observations is qualitatively excellent, correctly predicting, in particular, the dispersion of the up- and downstream propagating wave packets, the distance travelled by the packet as a whole, the phase propagation of individual crests and troughs and the dispersion of the packet.

For a more detailed examination of the motion and width of the wave packets propagating outward from the initial pulse centred at spatial position $\boldsymbol{r}_0 = (x_0, y_0)$, we

https://doi.org/10.1017/jfm.2019.424 Published online by Cambridge University Press

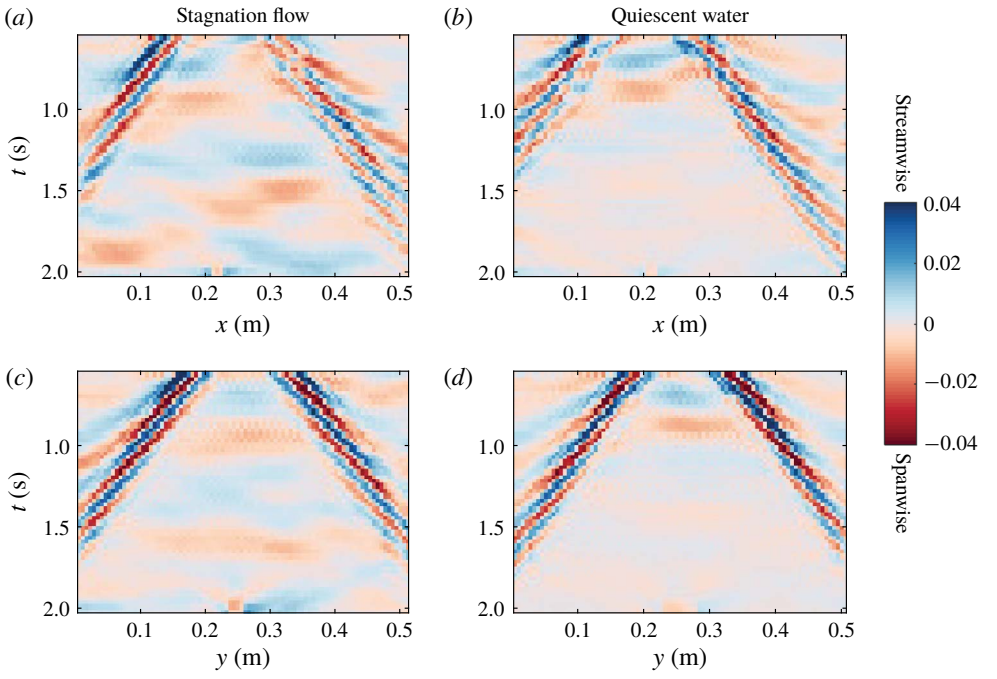


FIGURE 6. (Colour online) The measured surface gradient as a function of space and time for a ring wave atop the sub-surface shear current profile A in figure 2(*a*) (*a* and *c*), and in quiescent waters (*b* and *d*): (*a*,*b*) show the streamwise surface gradient component as a function of streamwise position x, along a line passing through the centre of the initial pressure pulse; (*c*,*d*) show the same, but for spanwise positions and gradient component. The colour bar applies to all panels.

consider figure 6, which shows the surface gradient components as a function along streamwise (figure 6*a*,*b*) and spanwise (figure 6*c*,*d*) lines passing through $\boldsymbol{r}_0$, showing positions upstream/downstream and orthogonally left and right of $\boldsymbol{r}_0$, respectively. Figures 6(*a*) and 6(*c*) are for the ring waves measured atop the stagnation region flow, figures 6(*b*) and 6(*d*) for quiescent water (the same measurements shown in the top and bottom rows of figure 4). Considering figure 6(*a*), it is clear that the downstream propagating wave packet (shear-assisted direction) is greater in spatial width than the upstream packet (shear-inhibited direction), evidencing the increased (decreased) dispersion in the shear-assisted (inhibited) direction, confirming theoretical predictions of Ellingsen (2014*b*). For wave motion along the same direction in quiescent waters in figure 6(*b*) as well as wave motion in the spanwise directions in figure 6(*c*,*d*), the spatial width of the wave packets in both directions is approximately the same.

The motion of the wave packet as a whole is determined by the group velocities of the relevant wavelengths, and is reflected by the slope of the packet as seen in figure 6, i.e. the translation of the packet in space over a given time interval. Also apparent in figure 6 are darker and lighter lines along which the surface gradient has maximum, or zero, absolute value, respectively. These represent the motion of constant wave phase (for instance crests and troughs), and their slope indicates the phase velocities. Considering figure 6(*a*), it is evident that while the group velocity is approximately the same in shear-assisted and shear-inhibited directions of

https://doi.org/10.1017/jfm.2019.424 Published online by Cambridge University Press

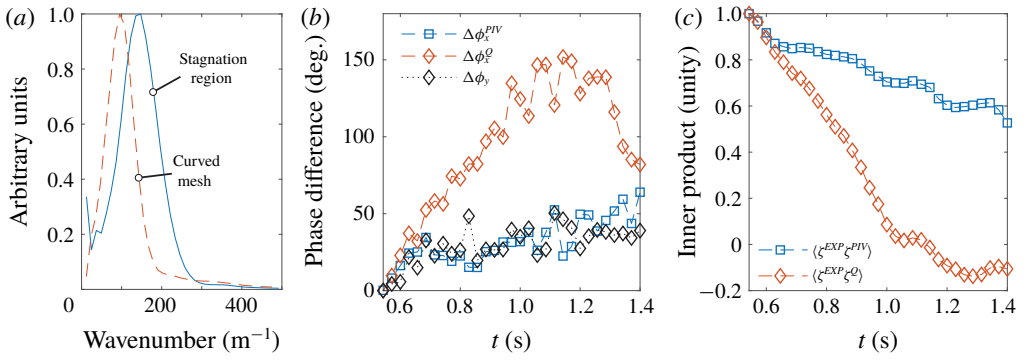


FIGURE 7. (Colour online) (*a*) Wavenumber spectrum for ring waves atop the curved mesh and stagnation region flows. (*b*) Weighted average phase difference between ring waves measured experimentally in the stagnation region and theoretical predictions: $\Delta\phi_x^{PIV}$ uses the dispersion relation for waves atop the shear profile as measured by PIV, considering waves along the x-direction; $\Delta\phi_x^{Q}$ is the same but using the quiescent-water dispersion relation; $\Delta\phi_y$ considers waves travelling in the y-direction perpendicular to the flow. (*c*) Normalized inner product (defined in the text) between experimentally measured surface elevation, and that predicted by theory using the dispersion relation reflecting the measured shear profile ($\langle\hat{\zeta}^{EXP}\hat{\zeta}^{PIV}\rangle$) and quiescent dispersion relation ($\langle\hat{\zeta}^{EXP}\hat{\zeta}^{Q}\rangle$). For (*b*,*c*), initial time $t_0 = 0.54$ s.

propagation, the difference between phase and group velocity is greater (smaller) in the shear-assisted (shear-inhibited) direction. This confirms the theoretical predictions of Ellingsen (2014*b*). In figure 6(*b–d*), the angular misalignment between lines representing the group and phase velocities is roughly the same in both propagation directions, as expected. Further and more quantitative analysis of the relationship between group and phase velocities for different propagation directions is given below in the discussion of figure 8.

We now proceed with some quantitative comparisons between the measured ring waves and theoretical predictions. For further use, we first define a wavenumber spectrum as:

$$S(k) = \int_0^{2\pi}\int_0^{\infty} \mathrm{d}\omega\,\mathrm{d}\theta(|P_x(\boldsymbol{k},\omega)|^2 + |P_y(\boldsymbol{k},\omega)|^2), \tag{5.1}$$

with $\boldsymbol{k} = k(\cos\theta, \sin\theta)$. The spectra $S(k)$ for the ring waves atop the stagnation region and curved mesh flow are shown in figure 7(*a*), in units normalized to the peak value. As can be seen, the peak spectral components of the curved mesh flow are centred at a smaller wavenumber, consistent with the pneumatic pulse being positioned at a greater height, thus producing a broader initial deformation of the surface.

The theoretical predictions for ring waves use the measured surface elevation ζ_0 and time derivative $\dot{\zeta}_0$ determined as in § 2.1 as initial conditions in (2.10), where ζ_0 and $\dot{\zeta}_0$ are taken at the earliest time t_0 where the measured ring wave patterns were unobstructed by the pneumatic pulse mounting apparatus. The surface elevation at other times was predicted using (2.9) and disregarding measurement errors in ζ_0 and $\dot{\zeta}_0$, the accuracy of the theoretical predictions is related to the determination of phase velocities $c_\pm(\boldsymbol{k})$. Errors in $c_\pm(\boldsymbol{k})$ result in wavelength components drifting out of phase with time after t_0, reflected by the complex phase factors in (2.9). To quantify this

https://doi.org/10.1017/jfm.2019.424 Published online by Cambridge University Press

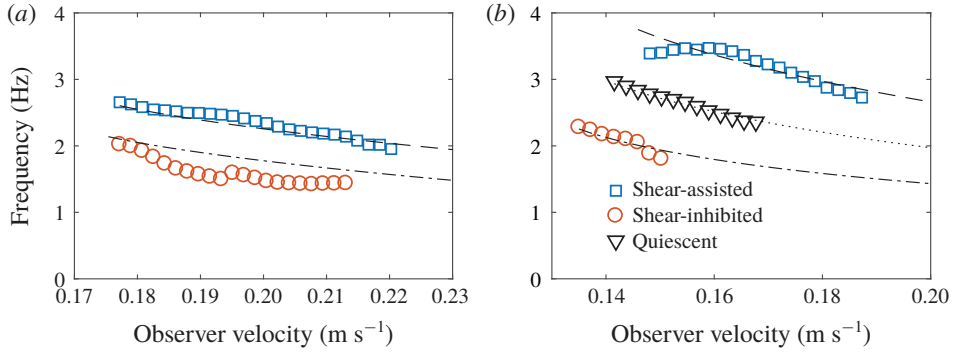


FIGURE 8. (Colour online) The frequency of waves travelling past an observer moving at a particular velocity outward from the position of the initial ring wave pulse, for the curved mesh flow (*a*) and stagnation region flow (*b*). Shear-assisted and shear-inhibited directions are considered, as well as the case of quiescent waters for the stagnation region. The legend applies to both (*a*) and (*b*).

phase shift and assess the accuracy of the theoretical predictions, we define weighted averaged phase differences between the measured surface elevation for ring waves in the stagnation region, $\hat{\zeta}^{EXP}$, and theoretical predictions with $c_{\pm}(\boldsymbol{k})$ calculated using the measured stagnation region shear profile ($\hat{\zeta}^{PIV}$) and predictions using the quiescent-water dispersion relation ($\hat{\zeta}^{Q}$):

$$\Delta\phi_x^{PIV}(t) = \int_{k_{0.5}} \mathrm{d}k S(k)\mathrm{Arg}[\zeta^{PIV}(k,0,t)\zeta^{EXP,*}(k,0,t)] \Big/ \int_{k_{0.5}} \mathrm{d}k S(k), \tag{5.2a}$$

$$\Delta\phi_x^{Q}(t) = \int_{k_{0.5}} \mathrm{d}k S(k)\mathrm{Arg}[\zeta^{Q}(k,0,t)\zeta^{EXP,*}(k,0,t)] \Big/ \int_{k_{0.5}} \mathrm{d}k S(k), \tag{5.2b}$$

$$\Delta\phi_y(t) = \int_{k_{0.5}} \mathrm{d}k S(k)\mathrm{Arg}[\zeta^{PIV}(0,k,t)\zeta^{EXP,*}(0,k,t)] \Big/ \int_{k_{0.5}} \mathrm{d}k S(k), \tag{5.2c}$$

where an un-hatted surface elevation quantity indicates a spatial Fourier transform as in (2.1), an asterisk indicates a complex conjugate, Arg[] is the complex phase angle and $k_{0.5}$ indicates integration over wavenumbers where $S(k)$ is greater than 50 % of the peak value. Here, ζ^{EXP}, ζ^{Q} and ζ^{PIV} are functions of (k_x, k_y, t), $\Delta\phi_x^{PIV}(t)$ represents the spectrally weighted phase difference between measured waves and theoretical predictions with $c_{\pm}(\boldsymbol{k})$ reflecting the measured phase velocity, for waves travelling along and against the streamwise direction ($k_y = 0$), $\Delta\phi_x^{Q}(t)$ is the same but using the quiescent-water dispersion relation in the theoretical predictions, $\Delta\phi_y(t)$ considers wave components propagating along the spanwise direction ($k_x = 0$), for which it is inconsequential which dispersion relation is used. The results for ring waves in the stagnation region are shown in figure 7(*b*); $\Delta\phi_x^{Q}$ initially increases at a much greater rate in time compared to $\Delta\phi_x^{PIV}$ and $\Delta\phi_y$, since the dispersion relation does not include the effects of the shear current. As the maximum phase difference defined here is 180°, which is a weighted average over different wavelength components drifting out of phase at varying rates in time, it is reasonable that the maximum of $\Delta\phi_x^{Q}$ does not reach 180°. The decay of $\Delta\phi_x^{Q}$ at larger times is likely due to wave components beginning to drift back in phase with the experimental

https://doi.org/10.1017/jfm.2019.424 Published online by Cambridge University Press

measurements. The rate of increase of $\Delta\phi_x^{PIV}$ and $\Delta\phi_y$ is roughly the same, likely caused by errors in the initial conditions used in (2.10) and by inhomogeneity of the dispersion relation across the measurement area in the stagnation region as discussed in § 3. Considering the peak wavenumber component in figure 7(*a*), a 2.5 % variation in wave phase velocity (and frequency) is expected over the measurement area due to the surface boundary layer development (see figure 2*c*), which corresponds to a $\sim 50^\circ$ degree phase lag over the time period of figure 7(*b*). This estimate is likely an upper bound considering that a wave does not propagate over the entire measurement area, yet is roughly the peak value of the phase lag for $\Delta\phi_x^{PIV}(t)$.

Another metric for quantifying the accuracy of theoretical predictions involves simply comparing the difference between predicted and measured surface elevations. We define the normalized inner product

$$\langle \hat{\zeta}^1 \hat{\zeta}^2 \rangle = \frac{\int \mathrm{d}\boldsymbol{r} \hat{\zeta}^1(\boldsymbol{r}) \hat{\zeta}^2(\boldsymbol{r})}{\sqrt{\int \mathrm{d}\boldsymbol{r} |\hat{\zeta}^1(\boldsymbol{r})|^2 \int \mathrm{d}\boldsymbol{r} |\hat{\zeta}^2(\boldsymbol{r})|^2}}, \tag{5.3}$$

where $\hat{\zeta}^1(\boldsymbol{r})$ and $\hat{\zeta}^2(\boldsymbol{r})$ are surface elevation functions of horizontal spatial coordinates at a particular time value. As for the phase differences, we consider theoretical predictions using dispersion relations with and without the effects of the subsurface shear current included. Inner products, between experimentally surface elevation and theoretical predictions as a function of time are shown in figure 7(*c*). The inner product with the theoretical prediction assuming a quiescent-water dispersion relation decays at a much higher rate than the case including the effects of shear currents, showing that the theoretical propagation in time of the initial perturbation is poor in the former case and far better in the latter. The necessity of taking shear effects of the dispersion into account is again confirmed.

As predicted theoretically and observed qualitatively in figure 6, the difference between wave group and phase velocities is anisotropic in the presence of a subsurface shear current. To quantify the effect in the context of the experimentally measured ring waves, we consider an observer travelling at a particular velocity V in a direction along the x-axis outward from the location of the initial pneumatic pulse $\boldsymbol{r} = (x_0, y_0)$. Presume that $V = C_g$ where C_g is the group velocity of a wave of wavenumber k_g. This observer would measure waves passing by at a frequency determined by the difference between group and phase velocities for the relevant wavelength. If the phase velocity in this direction for wavenumber k_g is C, the observed wave frequency is

$$(C - C_g)k_g. \tag{5.4}$$

The time-dependent wave amplitude $A(t)$ seen by the said observer for an experimentally measured ring wave is calculated as:

$$A(t) = \hat{\zeta}^{EXP}(x_0 + (U_0 \pm C_g)t, y_0, t), \tag{5.5}$$

where U_0 is the measured surface velocity of the shear current, the $+(-)$ sign for shear-assisted (inhibited) direction in the case of the stagnation region flow and opposite for the curved mesh flow and t is the time after the initial pulse. The velocity $V = C_g$ of the observer is defined relative to the surface velocity U_0.

https://doi.org/10.1017/jfm.2019.424 Published online by Cambridge University Press

The observed wave frequency is found by analysing $A(t)$ in the frequency domain and finding the peak frequency with a Gaussian fit. The observed wave frequency as a function of observer group velocity in the shear-assisted and shear-inhibited directions for ring waves in the curved mesh and stagnation region flows is shown in figure 8. The circles, squares and triangles represent the frequencies extracted from (5.5), while the dashed and dotted curves represent theoretical predictions based on the calculated dispersion relation and (5.4). Also shown in figure 8(*b*) is the quiescent-water case for which the frequencies are the same regardless of the direction of movement of the observer. The data points shown include only wavenumber components where $S(k_g)$ is greater than 50 % of the peak value. In both plots, the frequencies are higher for the shear-assisted cases, quantifying the predicted increased (decreased) difference between the phase and group velocities for the shear-assisted (inhibited) direction of motion, also evident in the curves in figure 3(*b*). It is noted that the frequency variation is due in part to the variation in k_g, which increases (decreases) for the shear-assisted (inhibited) direction. The frequencies for the quiescent-water case lie in between the shear-assisted and shear-inhibited cases as expected. Agreement with theoretical predictions is satisfactory in all cases.

6. Ship wave observations

Ship waves were measured in the stagnation flow region with a miniature Series 60 hull of length $L = 110$ mm and beam 16 mm for different values of the Froude number $Fr = V/\sqrt{gL}$ (V: velocity relative to the free surface) and three different angles relative to the stagnation current profile B in figure 2(*a*). We consider only waves behind the ship, as the capillary waves in front are at least partially obstructed by the ship towing apparatus, and predicted to be very small in wavelength given the values of the surface tension (see e.g. figure 3*b*), likely smaller than the spatial resolution of the synthetic schlieren system.

The results for ship motion in the shear-assisted and shear-inhibited directions are shown in figure 9, and for the cross-flow (90°) direction in figure 10. The measured waves behind the ship are shown in the blue-tinted panels (columns 1 and 3 from the left in figure 9 and column 1 in figure 10) at four different Froude numbers – $Fr = 0.3$, 0.4, 0.5 and 0.6 – one per row in the figures as indicated. Corresponding theoretical predictions based on the measured velocity profiles and surface tension using the theory described in § 2 are shown in the green-tinted panels (columns 2 and 4 of figure 9 and columns 2 and 3 of figure 10). The sub-surface flow is from left to right in all panels in both figures. The coefficient Γ in the stagnation region was measured to be $3.7 \pm 0.1 \times 10^{-5}$ m^3 s^{-2} for the experiments in figure 9 and $2.4 \pm 0.1 \times 10^{-5}$ m^3 s^{-2} for those in figure 10. For the theoretical predictions the ship was modelled as in § 2, equation (2.8). The theoretical model is fully transient to include the effects of the acceleration phase, using (2.5) for a moving pressure distribution. To facilitate a more quantitative comparison between the measured waves and theory, the theoretically predicted surface elevation is normalized such that the r.m.s. of the along-ship gradient component is equal to that measured experimentally. The colour bars in all panels show the surface elevation in millimetres.

A visual comparison shows satisfactory agreement with theoretical predictions. A number of predicted features are clearly visible. Most striking is the asymmetry of the patterns for ship motion at 90° in figure 10, predicted first by Ellingsen (2014*a*). The transverse waves (those directly behind the ship in the central region of the V-shaped wake pattern) make an angle to the direction of ship motion, differing from the

https://doi.org/10.1017/jfm.2019.424 Published online by Cambridge University Press

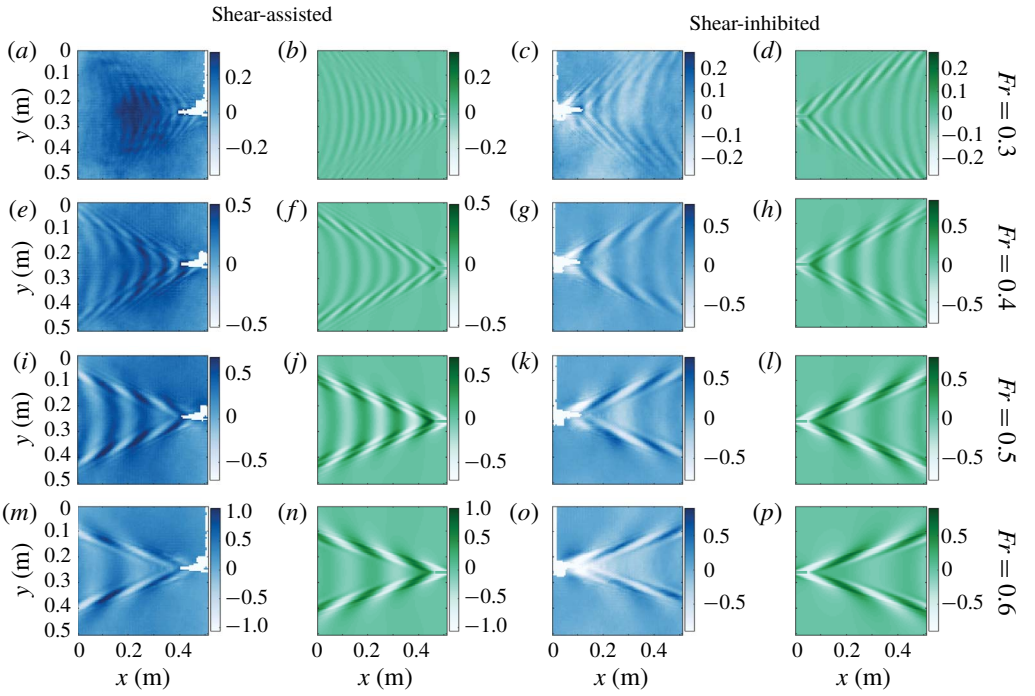


FIGURE 9. (Colour online) Ship waves in the stagnation flow region at Froude numbers 0.3, 0.4, 0.5 and 0.6 (rows 1–4 from the top, respectively), for ship motion in shear-assisted (columns 1 and 2 from the left), and shear-inhibited (columns 3 and 4) directions. Columns 1 and 3 are laboratory measurements (blue tinted); 2 and 4 are theoretical predictions (green tinted). In all panels the surface is at rest in the laboratory frame with sub-surface flow towards the right. The colour bars show the surface elevation in millimetres.

quiescent-water case as well as the shear-assisted and inhibited directions atop a shear flow. In addition, the width of the diverging wave packets at the boundaries of the wake pattern is wider on the port side of the ship (the right side in figure 10), most evident for the two highest Froude numbers. Both of the above phenomena are visible in the modelled ship wakes as well (column 2). Next, the wavelength of transverse waves is shortened (lengthened) for shear-assisted (inhibited) motion, and is correctly predicted in all graphs in figure 9.

The wavelength variation of the transverse waves confirms intuition considering the sub-surface shear currents as discussed by Ellingsen (2014*a*). For shear-assisted (inhibited) motion, the sub-surface flow is along (against) the direction of the transverse waves, increasing (decreasing) their phase velocity as seen in figure 3(*b*) (the same trends occur for shear profile B relevant here). Since $c(\boldsymbol{k})$ is a monotonically decreasing function of k in all directions, the wavelength of a wave having phase velocity equal to the ship speed might be expected to be shorter (longer), confirmed by considering the intersection of the phase velocity curves in figure 3(*b*) with a line of constant velocity. Differences between the measured and modelled ship wakes in figures 9 and 10 are largely attributed to the use of a pressure patch in modelling the ship hull. Firstly, the hyper-Gaussian pressure distribution has a different spatial distribution than the profile of the ship hull, resulting in different weighting of

https://doi.org/10.1017/jfm.2019.424 Published online by Cambridge University Press

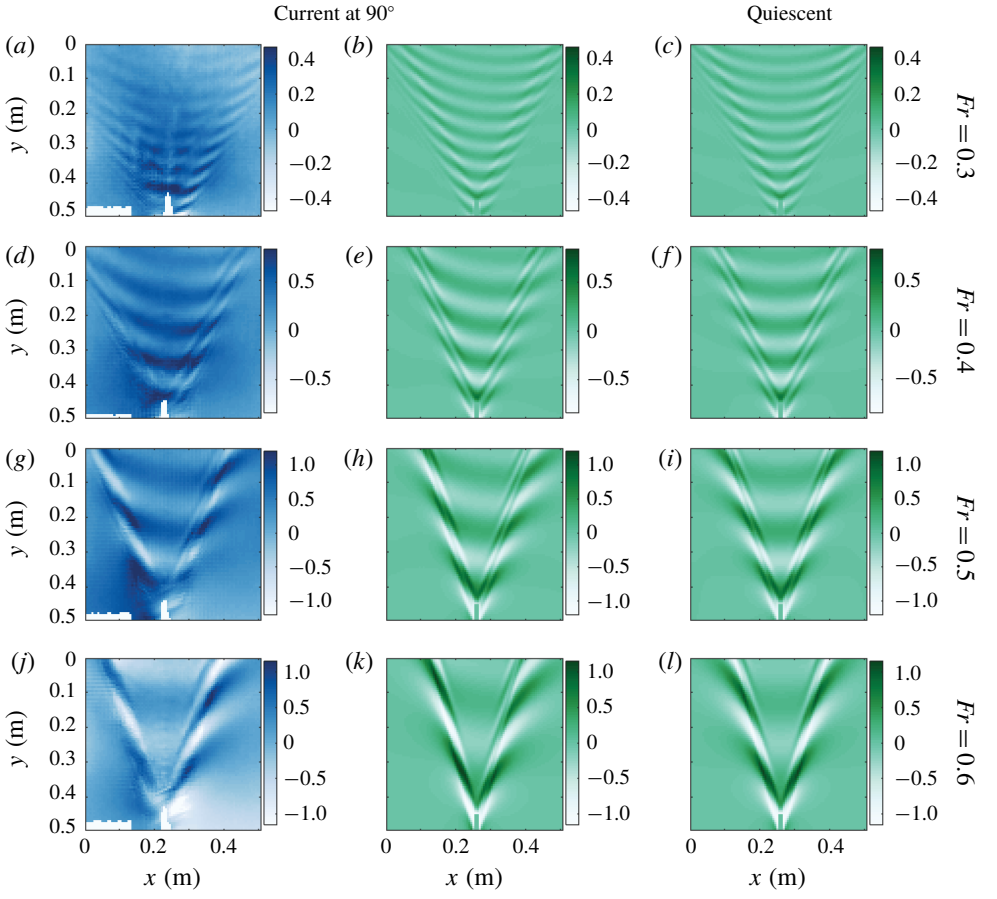


FIGURE 10. (Colour online) Ship waves in the stagnation flow region for motion in the cross-current direction at Froude numbers 0.3, 0.4, 0.5 and 0.6 (rows 1–4 from the top, respectively). Column 1 shows laboratory measurements (blue tinted); 2 shows theoretical predictions (green tinted). The theoretical prediction in quiescent waters is shown in column 3 for comparison. In all panels the surface is at rest in the laboratory frame with sub-surface flow towards the right. The colour bars show the surface elevation in millimetres.

various wavelength components reflected by the $p_{\mathrm{ext}}(\boldsymbol{k})$-term in (2.7). Secondly, once in motion the surface depression due to the pressure patch will no longer have exactly the same shape as the patch itself.

A more quantitative comparison can be made from the surface elevation transformed to Fourier space in the two spatial dimensions, by extracting and plotting the peak value of the along-ship (longitudinal) wavenumber $k_{\parallel}$ as a function of the cross-ship (transverse) wavenumber $k_{\perp}$ for each case, shown in figure 11. The far-field waves away from the ship are given by the poles where the denominator of (2.7) is zero, cf. Wehausen & Laitone (1960). The spectral peak values of $\boldsymbol{k}$ in figure 11 thus correspond to the solution to $c_{+}(\boldsymbol{k}) = 0$, the criterion for the waves to be stationary in the ship's system of reference. For a perfectly stationary ship wave pattern, only these $\boldsymbol{k}$-values can be present. Extraction is made from a frame average of video

https://doi.org/10.1017/jfm.2019.424 Published online by Cambridge University Press

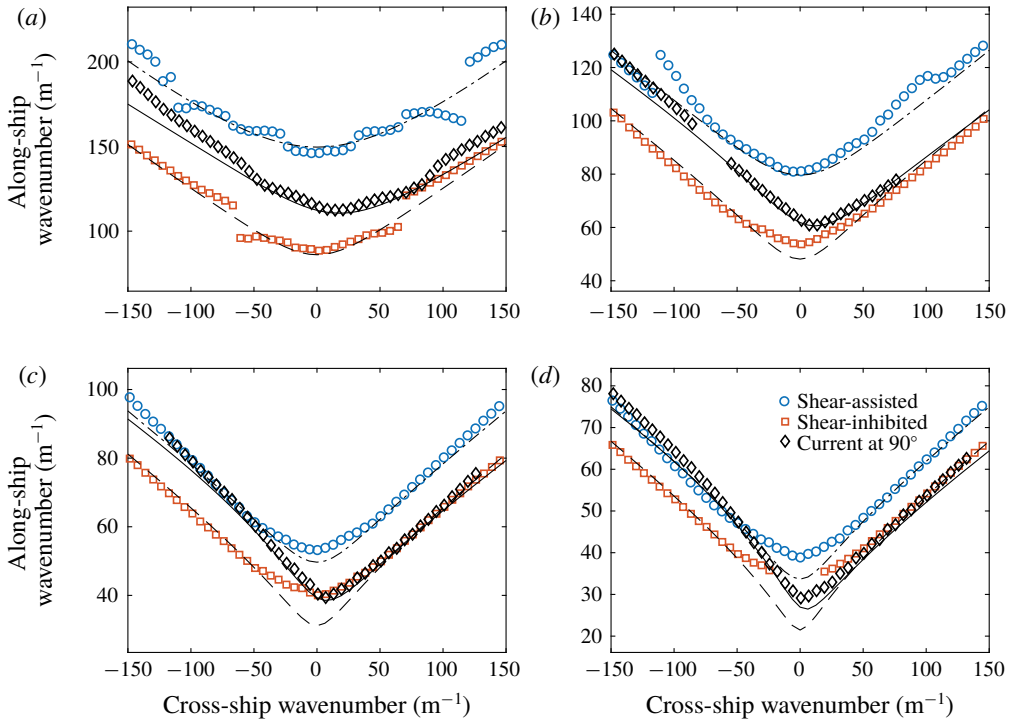


FIGURE 11. (Colour online) Dispersion curves for stationary ship waves in $\boldsymbol{k}$ space extracted from experimental measurements in figures 9 and 10 for $Fr = 0.3$ (*a*), 0.4 (*b*), 0.5 (*c*) and 0.6 (*d*) respectively. The legend applies to (*a–d*). The dashed and dotted lines show the theoretical predictions.

frames where the model ship is in the field of view of the camera, finding the peak along-ship wavenumber as a function of cross-ship wavenumber using a Gaussian fit of the frame-averaged surface elevation magnitude in Fourier space.

Several predicted qualitative properties observed visually in figures 9 and 10 are confirmed. For a given along-ship wavenumber $k_\parallel$, the cross-ship wavenumbers $k_\perp$ satisfying the stationary wave condition are consistently lower for SA than for SI ship motion, evidence that the dominant wave modes propagate at a larger angle relative to the line of motion. In particular, the higher value of $k_\parallel$ at $k_\perp = 0$ quantifies the shorter wavelength of transverse waves, which is also easy to see by eye. The curve of stationary phase is moreover highly asymmetrical for cross-current motion. The minimal value of the ratio is at a non-zero value of $k_\perp$, indicating that the transverse waves are skewed, as is indeed obvious in figure 10(*g*,*j*). We also plot the curves expected from theory, based on the numerically evaluated dispersion relation in the stagnation region (dashed and dotted lines).

The agreement is reasonably good overall, considering the limited spatial extent of the measurement area, and hence the limited resolution in $\boldsymbol{k}$ space. The exception is the smaller wavenumbers in figure 11(*c*,*d*) which we cannot measure accurately for this reason. Indications are also present that transient effects play a role for these longest wavelengths which appear in the transverse waves. For shear-inhibited motion in figure 9 the transverse wavelength of the last, rightmost period is visibly slightly shorter than for the transverse waves closest to the ship, a remnant of the ring wave

https://doi.org/10.1017/jfm.2019.424 Published online by Cambridge University Press

generated in the acceleration phase which the ship has not yet completely left behind. This would tend to give a higher value of k_x near $k_y = 0$, as observed for SI especially in figure 11(*c*,*d*) than that expected for a fully stationary ship wave pattern. The effect is greater for the two higher Froude numbers, where the average is taken over only two wavelengths of the transverse waves visible in the frame, whereas for lower Fr more wavelengths are present in the region where the ship waves have reached their stationary shape. At $Fr = 0.6$ the effect is evident to some extent for all directions of motion for the same reason.

Deviations for $Fr = 0.3$ and 0.4 cases in figure 11(*a*,*b*) are likely due to a lower signal-to-noise ratio caused by the smaller wave amplitudes, as well as variation in wave dispersion across the measurement area caused by the surface boundary layer development (see figure 2*b*), which increases for smaller Fr. Nonetheless, in most cases the deviations between experiment and theory are significantly less than the variations in the curves for different directions of ship motion, confirming the predicted trends. Furthermore, differences in $k_{\|}$ in the shear-assisted versus shear-inhibited directions is significantly greater than the estimated variation in wavenumber over the measurement domain from the surface boundary layer (5 % variation for $Fr = 0.3$ and 2 % for $Fr = 0.6$), ruling out the possibility that the trends are due to the boundary layer.

7. Concluding remarks

We have made laboratory observations of ring waves and ship waves distorted by a sheared current beneath the surface. Ring waves and ship waves were created pneumatically on a tailored shear current, and the surface elevation and shear profile were measured using a synthetic schlieren method and particle image velocimetry, respectively. In a region of strong shear beneath a stagnant surface (the Reynolds ridge phenomenon) very visible shear effects were observed, and effects are also clearly evident for a more weakly sheared, approximately depth-linear current created by a curved mesh at the flow inlet. Ring waves are clearly asymmetrical, and ship waves appear very different in shear-assisted, shear-inhibited and cross-current directions of motion, respectively. The results are compared to recently developed theory for linear surface waves on shear currents of arbitrary shear using the measured velocity profile as input, and the correspondence is qualitatively very satisfactory. In addition, a quantitative comparison of the dispersion curve for stationary ship waves in Fourier space reveals good correspondence considering the level of experimental accuracy.

Quantitative comparisons with theoretical predictions were performed for both ring waves and ship waves. The measured average phase shift for a ring wave is grossly mispredicted by no-shear theory, but in good agreement with predictions based on the measured shear current. Next, the wave frequency seen by an observer moving with the group velocity is shown to deviate sharply for upstream (shear inhibited for the stationary flow) versus downstream direction (shear assisted) for all shear flows in agreement with theory, while it conforms with theory for quiescent water for propagation normal to the shear current, also as expected.

Peak values of the measured two-dimensional Fourier spectrum for ship waves are shown to agree well with the predicted criterion of stationary ship waves, with the exception of some cases where results are imperfect due to the limited wavenumber resolution, transient effects and/or experimental noise. Once again the standard theory for quiescent water (or, equivalently, depth-uniform current) will cause gross misprediction.

https://doi.org/10.1017/jfm.2019.424 Published online by Cambridge University Press

None of these observed results would be present on a current which is uniform in depth.

Our results not only confirm theoretically predicted effects for these canonical surface wave patterns, but also lend strong empirical support to the reality of a range of profound real-life consequences. In particular, the same theory was recently used by Li *et al.* (2019) to predict wave resistance on ships in the Columbia river delta, finding a difference of a factor 3 in wave resistance for upstream versus downstream motion at the same velocity relative to the water surface, typical of smaller ships trafficking these waters. Also, highly significant lateral wave radiation forces as well as transient effects during manoeuvring were predicted. Similar conclusions for the case of hurricane waves were drawn long ago by Dalrymple (1973). The necessity of including shear effects in the calculation of wave loads and forces on vessels and installations is re-emphasized. There exists at present no practical and affordable design tool for predicting the three-way behaviour of physical systems involving both waves, moving bodies and shear currents: most calculational tools (e.g. the WAMIT toolkit Lee (1995)) are developed for potential flow and are inapplicable in the presence of shear (Ellingsen 2016), and computational fluid mechanics solving the full Euler or Navier–Stokes equations, as well as laboratory experiments with shear flow, are typically too costly and time consuming for design purposes, involving numerous parameters. An exception we are aware of is the CFDShip-Iowa code (Paterson, Wilson & Stern 2003) which, being a Navier–Stokes solver, allows rotational flow; no calculations appear to have been made for ship waves and loads on a shear current to date, however. The development of efficient predictive tools for wave–body–shear current behaviour should therefore be a priority in the near future.

Acknowledgements

S.Å.E. is funded by the Research Council of Norway (FRINATEK), grant no. 249740. Experiments were performed with the invaluable assistance of A. Ådnøy and S. Weichert. We thank an anonymous reviewer for suggesting the method used to measure the surface tension in the stagnation region.

Supplementary movie

Supplementary movie is available at https://doi.org/10.1017/jfm.2019.424.

REFERENCES

AKSELSEN, A. H. & ELLINGSEN, S. Å. 2018 Weakly non-linear transient waves on a shear current: ring waves and skewed Langmuir rolls. *J. Fluid Mech.* **863**, 114–149.

ALPERS, W. & HÜHNERFUSS, H. 1989 The damping of ocean waves by surface films: a new look at an old problem. *J. Geophys. Res.* **94**, 6251–6265.

BELCHER, S. E., GRANT, A. L. M., HANLEY, K. E., FOX-KEMPER, B., VAN ROEKEL, L., SULLIVAN, P. P., LARGE, W. G., BROWN, A., HINES, A., CALVERT, D. *et al.* 2012 A global perspective on Langmuir turbulence in the ocean surface boundary layer. *Geophys. Res. Lett.* **39**, L18605.

CAMPANA, J., TERRILL, E. J. & DE PAOLO, T. 2016 The development of an inversion technique to extract vertical current profiles from x-band radar observations. *J. Atmos. Ocean. Technol.* **33**, 2015–2028.

CAUCHY, A.-L. 1827 Théorie de la propagation des ondes à la surface d'un fluide pesant d'une profondeur indéfinie. *Mém. Présentés par Divers Savants Acad. Sci. Inst. Fr.* **1**, 3–123.

https://doi.org/10.1017/jfm.2019.424 Published online by Cambridge University Press

CAPLIER, C., ROUSSEAUX, G., CALLUAUD, D. & LAURENT, D. 2015 The effects of river counter-currents on ship wakes: an experimental approach. In *Proceedings of International Conference SHF and AICPN: Hydrodynamics and Simulation Applied to Inland Waterway and Port Approaches*. SHF (Société Hydrotechnique de France).

DALRYMPLE, R. A. 1973 Water wave models and wave forces with shear currents. *Tech. Rep.* 20. Coastal and Oceanographic Engineering Laboratory, Uni. Florida.

DARMON, A., BENZAQUEN, M. & RAPHAËL, E. 2014 Kelvin wake pattern at large Froude numbers. *J. Fluid Mech.* **738**, R3.

DUNN, W. & TAVOULARIS, S. 2007 The use of curved screens for generating uniform shear at low Reynolds numbers. *Exp. Fluids* **42**, 281–290.

ELIAS, E. P. L., GELFENBAUM, G. & VAN DER WESTHUYSEN, A. J. 2012 Validation of a coupled wave-flow model in a high-energy setting: the mouth of the Columbia River. *J. Geophys. Res.* **117**, C09011.

ELLINGSEN, S. Å. 2014*a* Ship waves in the presence of uniform vorticity. *J. Fluid Mech.* **742**, R2.

ELLINGSEN, S. Å. 2014*b* Initial surface disturbance on a shear current: the Cauchy–Poisson problem with a twist. *Phys. Fluids* **26**, 082104.

ELLINGSEN, S. Å. 2016 Oblique waves on a vertically sheared current are rotational. *Eur. J. Mech (B/Fluids)* **56**, 156–160.

ELLINGSEN, S. Å. & LI, Y. 2017 Approximate dispersion relations for waves on arbitrary shear flows. *J. Geophys. Res.: Oceans* **122**, 9889–9905.

FALTINSEN, O. M. 2005 *Hydrodynamics of High-Speed Marine Vehicles*. Cambridge University Press.

FIENUP, J. R. 1982 Phase retrieval algorithms: a comparison. *Appl. Opt.* **21**, 2758–2769.

HARPER, J. F. & DIXON, J. N. 1974 The leading edge of a surface film on contaminated flowing water. In *Proceedings of 5th Australasian Conference on Hydraulics and Fluid Mechanics*, pp. 499–505. University of Canterbury.

JOHNSON, R. S. 1990 Ring waves on the surface of shear flows: a linear and nonlinear theory. *J. Fluid Mech.* **215**, 145–160.

KHUSNUTDINOVA, K. R. & ZHANG, X. 2016 Long ring waves in a stratified fluid over a shear flow. *J. Fluid Mech.* **794**, 14–44.

KUMAR, N., VOULGARIS, G. & WARNER, J. C. 2011 Implementation and modification of a three-dimensional radiation stress formulation for surf zone and rip-current applications. *Ocean Mod.* **47**, 1097–1117.

LEE, C.-H. 1995 *WAMIT Theory Manual*. Massachusetts Institute of Technology, Department of Ocean Engineering.

LI, Y. & ELLINGSEN, S. Å. 2016 Ship waves on uniform shear current at finite depth: wave resistance and critical velocity. *J. Fluid Mech.* **791**, 539–567.

LI, Y. & ELLINGSEN, S. Å. 2019 A framework for modelling linear surface waves on shear currents in slowly varying waters. *J. Geophys. Res.: Oceans* **124**, 2527–2545.

LI, Y., SMELTZER, B. K. & ELLINGSEN, S. Å. 2018 Transient wave resistance upon a real shear current. *Eur. J. Mech. (B/Fluids)* **73**, 180–192.

LUND, B., GRABER, H. C., TAMURA, H., COLLINS, C. O. & VARLAMOV, S. M. 2015 A new technique for the retrieval of near-surface vertical current shear from marine X-band radar images. *J. Geophys. Res.: Oceans* **120**, 8466–8496.

MOISY, F., RABAUD, M. & SALSAC, K. 2009 A synthetic Schlieren method for the measurement of the topography of a liquid interface. *Exp. Fluids* **36**, 1021–1036.

NOBLESSE, F., HE, J., ZHU, Y., HONG, L., ZHANG, C., ZHU, R. & YANG, C. 2014 Why can ship wakes appear narrower than Kelvin's angle? *Eur. J. Mech. (B/Fluids)* **46**, 164–171.

PATERSON, E. G., WILSON, R. V. & STERN, F. 2003 *General-Purpose Parallel Unsteady RANS Ship Hydrodynamics Code: CFDSHIP-IOWA*. Iowa Institute of Hydraulic Research.

PEREGRINE, D. H. 1976 Interaction of water waves and currents. *Adv. Appl. Mech.* **16**, 9–117.

PETHIAGODA, R., MCCUE, S. W. & MORONEY, T. J. 2014 What is the apparent angle of a Kelvin ship wave pattern? *J. Fluid Mech.* **758**, 468–485.

POISSON, S.-D. 1818 Mémoire sur la théorie des ondes. *Mem. Prés. divers Savants Acad. Roy. Sci. Inst.* **1**, 70–186.

https://doi.org/10.1017/jfm.2019.424 Published online by Cambridge University Press

RABAUD, M. & MOISY, F. 2013 Ship wakes: Kelvin or Mach angle? *Phys. Rev. Lett.* **110**, 214503.

SCOTT, J. C. 1982 Flow beneath a stagnant film on water: the Reynolds ridge. *J. Fluid Mech.* **116**, 283–296.

SHRIRA, V. I. 1993 Surface waves on shear currents: solution of the boundary-value problem. *J. Fluid Mech.* **252**, 565–584.

SMELTZER, B. K. & ELLINGSEN, S. Å. 2017 Surface waves on arbitrary vertically-sheared currents. *Phys. Fluids* **29**, 047102.

STEWART, R. J. & JOY, J. W. 1974 HF radio measurements of surface currents. *Deep Sea Res. Ocean. Abstracts* **21**, 1039–1049.

THOMSON, S. W. 1887 On ship waves. *Proc. Inst. Mech. Engrs* **38**, 409–434.

WEHAUSEN, J. W. & LAITONE, E. V. 1960 Surface waves. In *Fluid Dynamics III* (ed. S. Flügge), Encyclopedia of Physics, vol. IX, pp. 446–778. Springer.

WILLERT, C., STASICKI, B., KLINNER, J. & MOESSNER, S. 2010 Pulsed operation of high-power light emitting diodes for imaging flow velocimetry. *Meas. Sci. Technol.* **21**, 075402.

ZIPPEL, S. & THOMSON, J. 2017 Surface wave breaking over sheared currents: observations from the mouth of the Columbia River. *J. Geophys. Res.: Oceans* **122**, 3311–3328.

https://doi.org/10.1017/jfm.2019.424 Published online by Cambridge University Press